Experimental Section

Preparation of electrolytes and electrodes:

Different amounts of taurine (0.1, 0.2, and 0.3 M) were successively dissolved in the blank electrolyte (blank, 3.5wt% NaCl) to obtain a series of electrolytes, which are denoted as blank, 0.1 M Tau, 0.2 M Tau, 0.3 M Tau, respectively.

Structural Characterization:

Electrolyte conductivity measurements were conducted using a conductivity meter (DDS-11A, China). The contact angle between the electrolyte and the magnesium anode was precisely captured by a contact angle meter (DSA25, Germany). To characterize the structure and chemical bonds, Fourier transform infrared (FT-IR) spectroscopy (utilizing an AVATAR 370 spectrometer), nuclear magnetic resonance (NMR) spectroscopy (employing a Bruker 400 MHz spectrometer, Germany), and Raman spectroscopy (using a Horiba LabRAM HR Evolution system equipped with a 532 nm laser) were employed. The pH values were obtained by a pH meter (Lichen, China). Surface element states were investigated by an X-ray photoelectron spectrometer (XPS, Thermo ESCALAB 250XI, USA). The morphologies of Mg anodes were studied by Field emission scanning electron microscope (SEM, TESCAN MIRA3, Czechia). The in situ optical microscopy was carried out using a homemade cell and an optical microscope equipped with a digital camera (Yalian, China).

Electrochemical Measurements and Tests:

Battery assembly: The air cathode (Youtoke, China) was fabricated by water transport permeable layer, current collector, and manganese dioxide catalytic layer. The exposed area of the anode was 1 cm^2. To ensure that the cathode had sufficient active sites for the oxygen reduction reaction, the exposed area of the cathode was enlarged to 9 cm^2. The electrochemical performance of aqueous Mg-air batteries was tested using a CT3001A multichannel galvanostat (Wuhan Land, China), and the ambient temperature of the battery was maintained at 25 °C. Additionally,

the discharge products were removed using a chromic acid solution containing 20 g CrO_3 and 1 g $AgNO_3$/100 mL. The anode efficiency, specific capacity, and energy density were calculated using the mass loss method and corresponding formulas mentioned in previous work. Electrochemical Impedance Spectroscopy (EIS) measurements were conducted at the Open Circuit Potential (OCP) utilizing an alternating current (AC) signal within the frequency range of 10^5 Hz to 10^{-2} Hz. The amplitude of the AC signal was precisely set at 5 mV. For impedance data analysis, an equivalent circuit model was fitted to the measurements using ZsimpWin software, enabling accurate interpretation of the EIS results. Furthermore, Potentiodynamic Polarization (PDP) tests were performed by scanning a potential range of ±500 mV relative to the OCP at a rate of 1 mV/s. The correlation results were obtained through Tafel fitting analysis, providing valuable insights into the electrochemical behavior of the system. Linear sweep voltammetry (LSV) measurement was performed at a scan rate of 1 $mV \cdot s^{-1}$ using three-electrode (Stainless steel sheet, Stainless steel sheet, and saturated calomel electrode as the working, counter, and reference electrodes, respectively). All the EIS, PDP, and LSV, curves were collected on the CorrTest electrochemical workstation (CorrTest, China)

Density Functional Theory (DFT) calculations

All Density Functional Theory (DFT) calculations were conducted utilizing the DMol^3 software.[1] The exchange-correlation function adopted was the Generalized Gradient Approximation (GGA)[2] in the Perdew-Burke-Ernzerhof (PBE) formulation, augmented with the DFT-D3 correction to account for dispersive interactions. A double numeric plus polarization (DNP) basis set[3] was employed to characterize the electronic structure of the systems under investigation. During the calculations, the convergence threshold for the electron self-consistent field (SCF) was established at 10^{-6} eV, with a thermodynamic dispersion value of 0.005 Hartree (Ha) applied to expedite SCF convergence. The energy, force, and displacement convergence criteria were rigorously set for geometrical optimization at 1×10^{-5} Ha, 0.002 Ha $Å^{-1}$, and 0.005 $Å^{-1}$, respectively. To precisely calculate the adsorption energies

of various molecules on the Mg crystallographic surface, a k-point sampling interval[4] of 0.023 $Å^{-1}$ was implemented, and a vacuum layer of 15 Å was introduced between slabs to minimize interslab interactions, ensuring accurate adsorption energy determinations.[5]

Binding energies were determined according to the formula: $E_{A-B} = E_{Total} - E_A - E_B$, where E_{A-B} represents the binding energy, E_{Total} is the total energy of the system, and E_A and E_B are the energies of molecules A and B, respectively.[6]

Molecular Dynamics (MD) Simulations

MD simulations were performed using the Forcite module to investigate the solvation structure of Mg^{2+} ions and hydrogen bonding in $MgCl_2$ electrolytes, both with and without additives. The $MgCl_2$ electrolyte model comprised 8 $MgCl_2$ units and 550 H_2O molecules, while the model with additives included 8 $MgCl_2$ units, 5 Tau molecules, and 550 H_2O molecules. The COMPASS III force field assigned charges to Mg^{2+}, Cl^-, additive molecules, and H_2O. Initial geometrical optimization was carried out in the Forcite module, followed by 20 annealing cycles in the temperature range of 300 to 500 K. Geometrical optimization was performed after each annealing step to obtain the lowest-energy conformation. Subsequently, NPT MD simulations were conducted for 10 ns at 298 K for the optimized geometries.

The MD simulations were executed in a three-dimensional box with periodic boundary conditions, keeping the surface atoms fixed. The model encompassed four layers of magnesium surface, along with 1100 water molecules, 16 $MgCl_2$ units, and 10 Tau molecules in the electrolyte region. The simulations were performed under canonical ensemble (NVT) conditions. Before the main simulations, the system[7,8] was pre-equilibrated using the Nose-Hoover method[9,10] at 700 K for 100 ps to attain a reasonable initial configuration. This was followed by a 5 ns simulation at 300 K using the Nose-Hoover thermostat method, with a time step of 1 fs.

All simulations were conducted with standard periodic boundary conditions, and both van der Waals and electrostatic interactions were cut off at 12.5 Å. Based on the MD simulation results, radial distribution functions

(RDFs)[11] were calculated using the analysis tools.

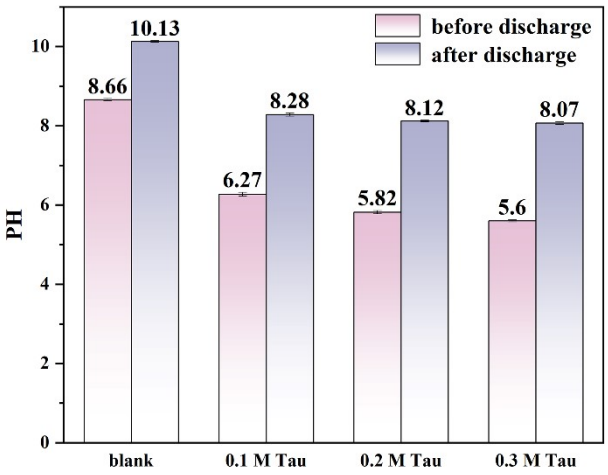

Fig. S1 Changes in pH before and after discharge of electrolytes containing different concentrations of additives.

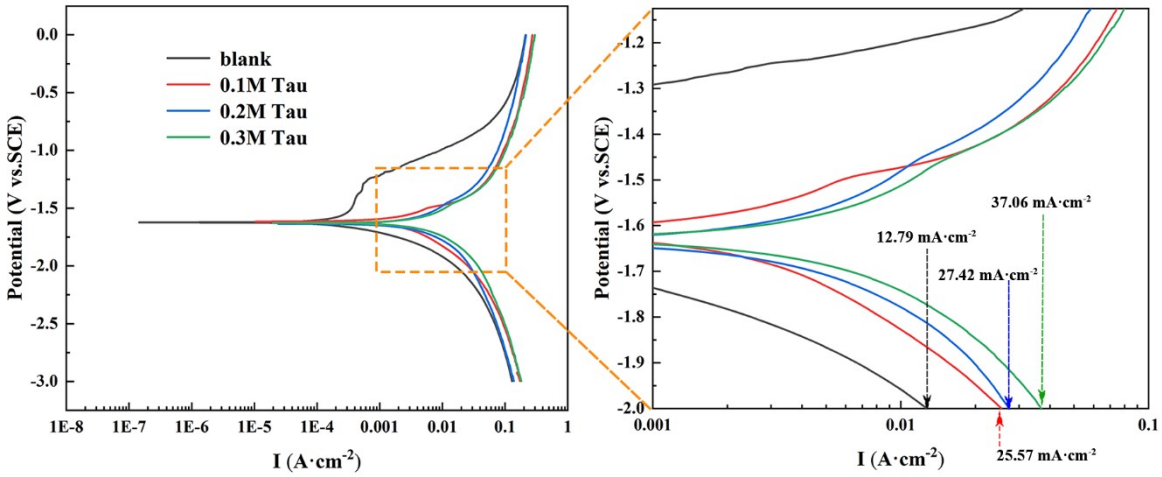

Fig. S2. Potentiodynamic polarization curves of AZ31 alloy in blank electrolyte and electrolytes with taurine at various concentrations.

Table S1 Charge transfer of three models calculated through Mullikens charge population analysis.

model	Mg-Tau-parallel	Mg-Tau-vertical1	Mg-Tau-vertical2	Mg-H_2O
Electron loss in magnesium slab	0.139	0.064	0.118	–0.021

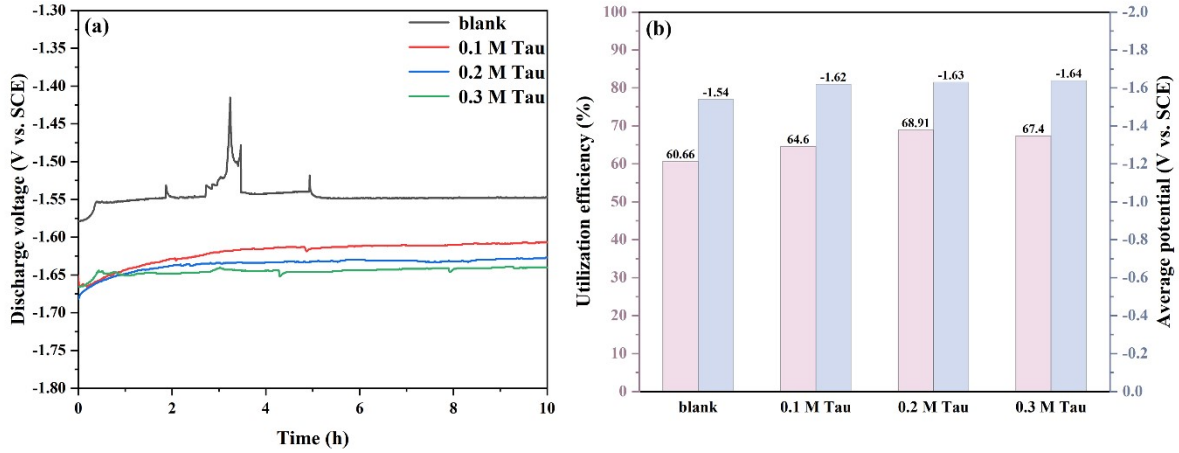

Fig. S3. Half-cell discharge performance assessment of AZ31 alloy in blank electrolyte and electrolytes doped with various concentrations of taurine: (a) discharge profiles and (b) utilization efficiency and average discharge potential of AZ31. (Test conditions: applied current density of 5 mA·cm^{-2}).

Table S2 Fitted parameters derived from electrochemical impedance spectroscopy for the anode in blank electrolyte.

additive	R_s	CPE_{dl}		R_{ct}	R_L	L
	Ω·cm^2	Y_1/μΩ^{-1}·cm^{-2}·s^n	n_1	Ω·cm^2	Ω·cm^2	H·cm^2
0 h	11.67	12.9	0.99	78.97	33.38	34.3
2 h	12.51	123.3	0.92	193.5	192.3	159.9
5 h	14.15	128.8	0.88	221.9	294.1	187.0
10 h	10.27	111.7	0.89	223.8	369.2	220.6

Table S3 Fitted parameters derived from electrochemical impedance spectroscopy for the anode in various electrolyte formulations.

additive	Time	R_s	R_f	CPE_f		R_{ct}	CPE_{dl}		R	L
				Y_1/μΩ^{-1}·cm^{-2}·s^n	n_1		Y_1/μΩ^{-1}·cm^{-2}·s^n	n_2		
0.1 M Tau	0 h	7.75	26.88	20.63	94.26	14.33	1.94×10^4	75.53	4.02	24.65
	2 h	8.35	29.76	24.68	93.39	14.64	1.71×10^4	92.86	14.62	58.31
	5 h	7.85	27.19	25.46	92.37	41.34	1.56×10^4	87.87	262.40	558.4
	10 h	7.05	45.07	25.97	92.34	22.85	1.11×10^4	80.00	369.20	220.6
0.2 M Tau	0 h	11.65	8.01	23.25	94.75	4.95	2.22×10^4	77.49	100	5.52
	2 h	12.63	10.00	32.24	89.83	17.56	2.24×10^4	74.06	6.28	172.80
	5 h	12.38	20.87	25.34	92.88	8.46	9.70×10^3	98.04	91.18	77.85
	10 h	18.83	22.96	27.76	91.64	13.87	2.24×10^4	62.17	3.24	26.67
0.3 M Tau	0 h	17.98	5.10	12.55	99.98	8.55	1.01×10^4	51.23	6.80	18.68
	2 h	13.23	11.38	31.26	90.63	6.01	1.65×10^4	85.38	13.05	10.01
	5 h	11.67	13.33	31.11	90.96	8.17	2.42×10^4	64.16	15.54	13.22
	10 h	10.61	12.96	30.35	92.56	15.51	9.58×10^3	99.95	17.40	12.56

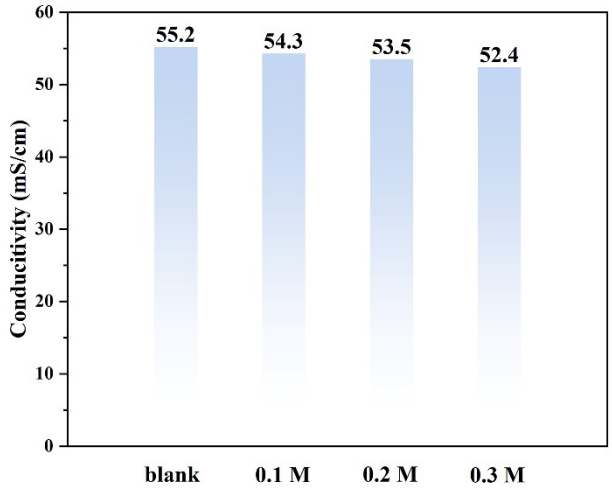

Fig. S4. Ionic conductivity of various electrolyte formulations.

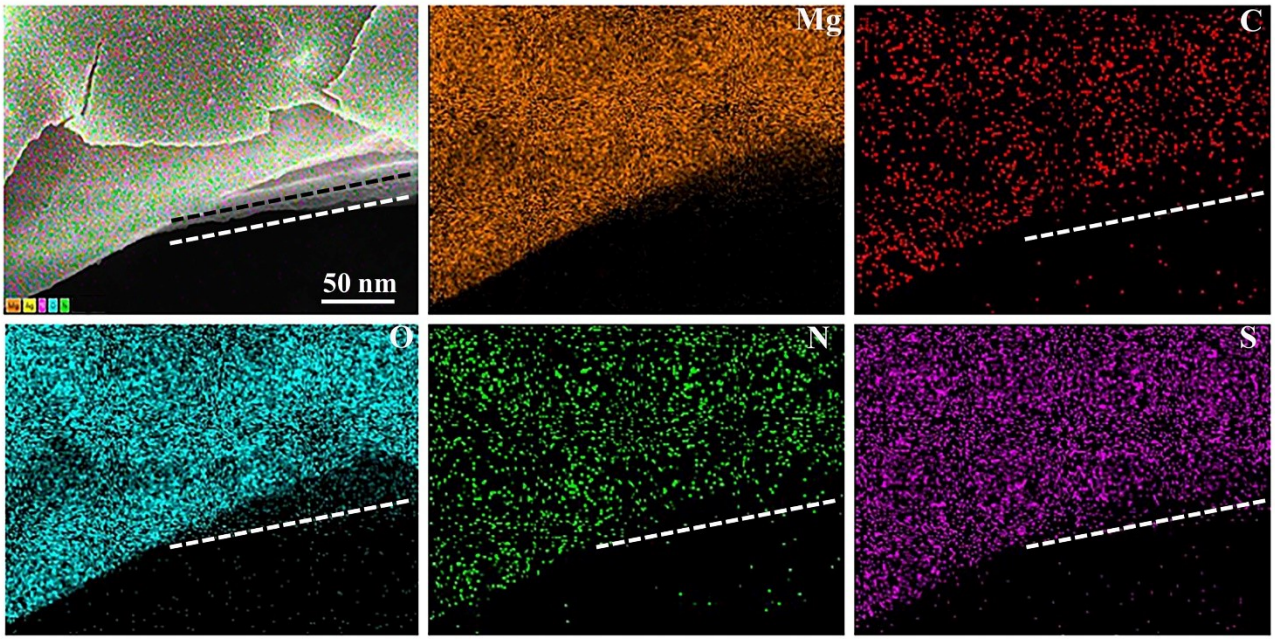

Fig. S5 SEM images and corresponding elemental maps of the magnesium anode after discharge in an electrolyte containing Tau additive.

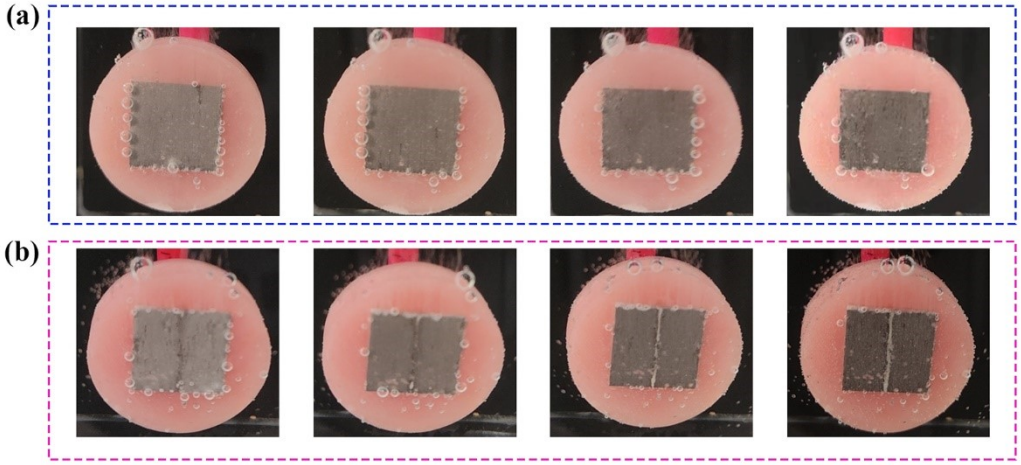

Fig. S6. Morphological evolution of anodes in electrolytes of differing durations, visualized through in situ endoscopic techniques: (a) blank; (b) 0.2 M Tau.

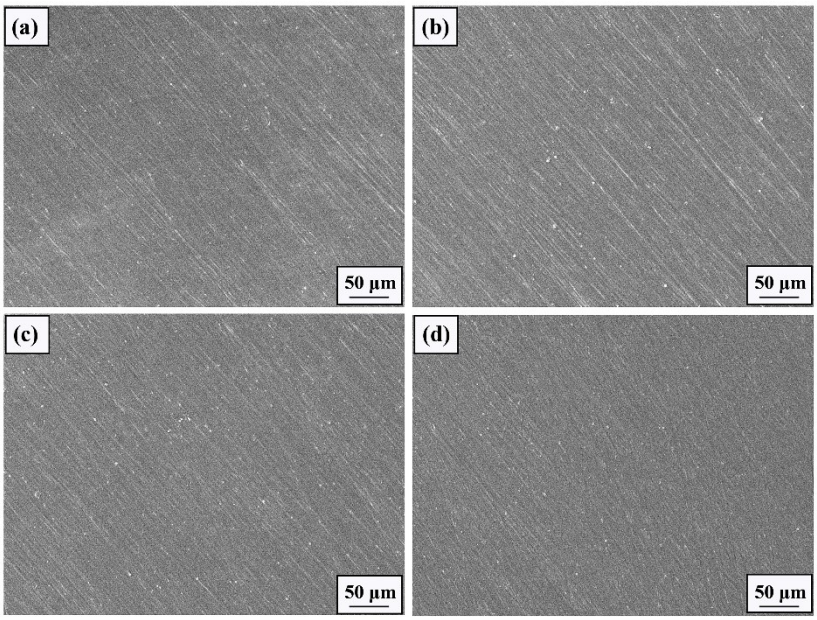

Fig. S7. The surface morphologies of the AZ31 anodes before intermittent discharge tests

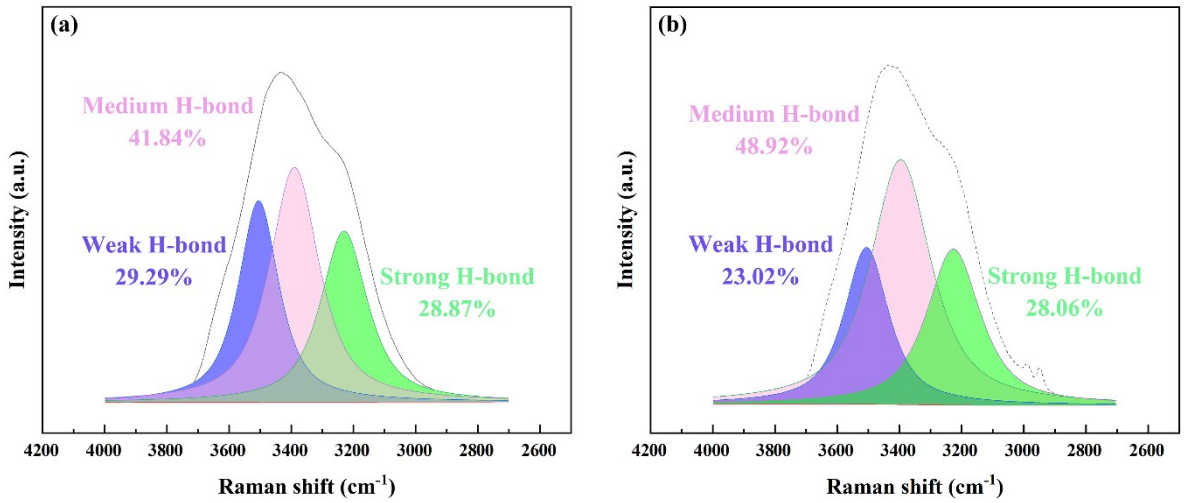

Fig. S8. Raman spectra of (a) blank and (b) 0.2 M Tau-containing electrolytes, fitted with three peaks corresponding to the O–H stretching vibrations of H_2O molecules in weak, medium, and strong hydrogen-bond states.

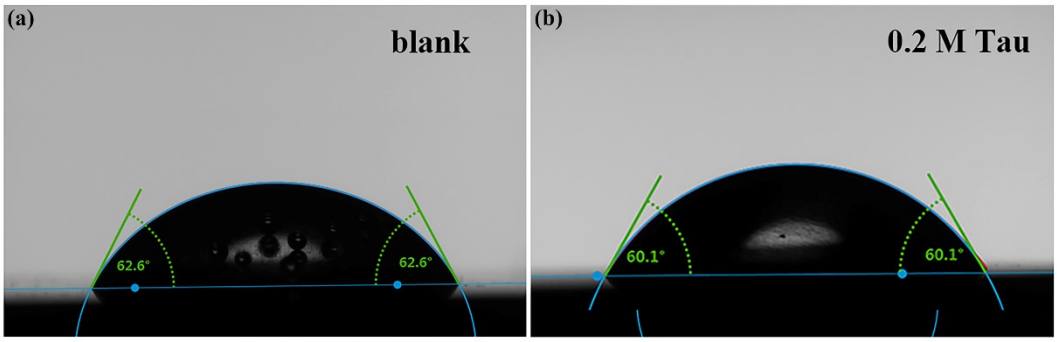

Fig. S9. Contact angle measurements between magnesium substrates and different electrolyte formulations.

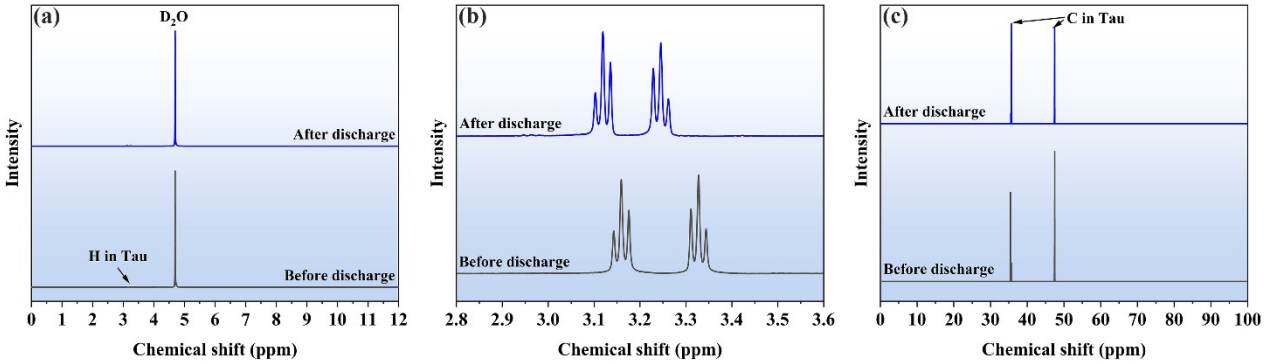

Fig. S10. (a) ^{1}H proton, (b) Localized ^{1}H NMR, and (c) ^{13}C NMR spectra of 0.2 M Tau electrolyte before and after discharge period.

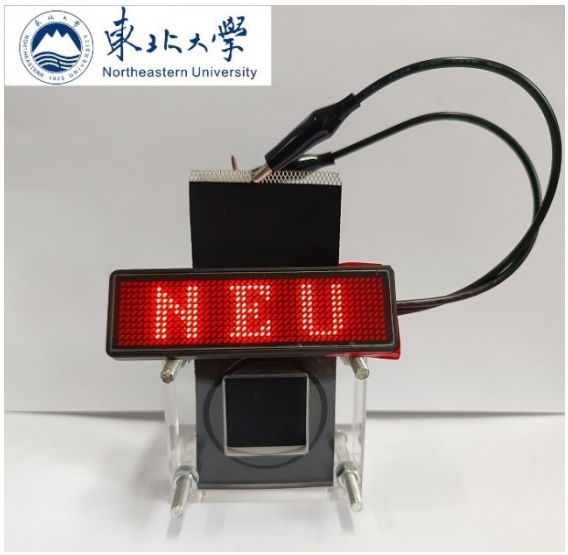

Fig. S11. LED signboard lighted by the Mg-air batteries added Tau/NaCl electrolytes.

References:

1 B. Delley, From Molecules to Solids with the DMol3 Approach, *J. Chem. Phys,* 2000, **113**, 7756–7764.

2 J. P. Perdew, K. Burke and M. Ernzerhof, Generalized Gradient Approximation Made Simple. *Phys. Rev. Lett.* 1996, **77**, 3865–3868.

3 B. Delley, An All-electron Numerical Method for Solving the Local Density Functional for Polyatomic Molecules, *J. Chem. Phys.,* 1990, **92**, 508–517.

4 H. J. Monkhorst, J. D. Pack, Special Points for Brillouin-Zone Integrations, *Phys. Rev. B,* 1976, **13** , 5188–5192.

5 S. Grimme, Semiempirical GGA-type density functional constructed with a long-range dispersion correction, *J. Comput. Chem,.* 2006, **27**, 1787–1799.

6 X. Yin, H. Wang and E.-H. Han, Effects of Solvation and Applied Potential on the Adsorption Behaviors of H, O, OH and H2O on Fe(110) Surface, *Surf. Sci.,* 2020, **691**, 121504.

7 A. D. MacKerell, D. Bashford and M. Bellott, All-Atom Empirical Potential for Molecular Modeling and Dynamics Studies of Proteins, *J. Phys. Chem. B,* 1998, **102**, 3586–3616.

8 H. Wang, H. Yuan, J. Wang, E. Zhang, M. Bai, Y. Sun, J. Wang, S. Zhu, Y. Zheng and S. Guan, Influence of the Second Phase on Protein Adsorption on Biodegradable Mg Alloys' Surfaces: Comparative Experimental and Molecular Dynamics Simulation Studies, *Acta Biomater.,* 2021, **129**, 323–332.

9 W. G. Hoover, Canonical Dynamics: Equilibrium Phase-Space Distributions, *Phys. Rev. A,* 1985, **31**, 1695–1697.

10 S. Nosé, A Unified Formulation of the Constant Temperature Molecular Dynamics Methods, *J. Chem. Phys.,* 1984, **81**, 511–519.

11 A. Stukowski, Visualization and Analysis of Atomistic Simulation Data with OVITO–the Open Visualization Tool, *Model. Simul. Mater. Sci. Eng.* 2010, **18**, 015012.